Modeling mechanochemical coupling in cell polarity establishment

Ondrej Maxian

October 31, 2023

This project is about understanding the design principles by which cells combine mechanics (the actomyosin network) and biochemistry to robustly polarize.

1 Dynamics of myosin in the embryo

We begin by considering a model of myosin by itself, to determine if it can spontaneously polarize. Spontaneous polarization of myosin, if possible, would explain the maintenance-phase rescue experiments that we observe.

1.1 Myosin as a self-patterning material

Let us begin by building a toy model for myosin dynamics. This section is a summary of the paper [2], which considers the same problem. The novelty in what we do will come later, when we couple myosin to branched actin and other proteins.

We describe the dynamics of myosin $M(x,t)$ using the advection-diffusion equation

$$\partial_t M + \partial_x (vM) = D_M \partial_x^2 M. \tag{1}$$

The complication is that the myosin is advected through a velocity field of its own making. The velocity field comes from stress generated in the fluid,

$$\sigma = \eta \partial_x v + \sigma_a(M), \tag{2}$$

which is a combination of viscous stress and active stress. As in [2], we ignore the elastic part of the stress, assuming the actomyosin cortex is purely viscous when in reality it is visco-elastic. The force balance equation in the fluid says that the force due to stress must be balanced by the drag force,

$$\gamma v = \partial_x \sigma, \tag{3}$$

1

where γ is the drag coefficient. Combining the force balance (3) with the stress expression (2) gives an auxillary equation for the velocity field

$$\gamma v = \eta \partial_x^2 v + \partial_x \sigma_a(M) \tag{4}$$

which couples to the myosin equation (1) via the active stress.

The advection-diffusion equation (1) is mass-preserving, meaning that the uniform steady state is just given by $M_0 = \dfrac{1}{L} \displaystyle\int_0^L M(x,0)\,dx$. For the active stress, we let $\sigma_a = \sigma_0 \hat{\sigma}_a(M)$. The analysis of [2] shows that (for periodic boundary conditions) the uniform steady state is unstable when

$$\text{Pe} \times \frac{M_0 \left(\partial_M \hat{\sigma}_a\left(M_0\right)\right)}{1 + (2\pi\ell/L)^2} > 1, \tag{5}$$

where $\ell = \sqrt{\eta/\gamma}$ is the characteristic lengthscale over which velocity decays (the diffusive lengthscale for velocity), L is the system length, and the Peclet number

$$\text{Pe} = \frac{\sigma_0}{D_M \gamma} \tag{6}$$

expresses the ratio of advective transport to diffusive transport. Qualitatively, the system has a uniform steady state and a second peaked steady state, where advective flux into the peaks matches the diffusive flux into the peaks. For this steady state to be stable, the advective transport must be sufficiently large relative to diffusive transport, so the Peclet number must be sufficiently large.

1.2 Myosin pattern formation with turnover

We now introduce a single species model of myosin with turnover,

$$\partial_t M + \partial_x \left(vM\right) = D_M \partial_x^2 M + k_M^{\text{on}} M_{\text{cyto}} - k_M^{\text{off}} M \tag{7a}$$

$$\gamma v = \eta \partial_x^2 v + \partial_x \sigma_a(M) \tag{7b}$$

$$M_{\text{cyto}} = \frac{1}{hL} \left(M^{(\text{Tot})} L - \int_0^L M(x)\,dx \right) \tag{7c}$$

It will be useful to nondimensionalize this equation, using the scalings

$$x = \hat{x}L \qquad t = \hat{t}/k_M^{\text{off}} \qquad M = \hat{M}M^{(\text{Tot})} \qquad v = \hat{v}\frac{\sigma_0}{\sqrt{\eta\gamma}} \tag{8}$$

The resulting equations are

$$\partial_{\hat{t}}\hat{M} + \hat{\sigma}_0 \partial_{\hat{x}} \left(\hat{v}\hat{M} \right) = \hat{D}_M \partial_{\hat{x}}^2 \hat{M} + \hat{K}_M^{\text{on}} \left(1 - \int_0^1 \hat{M}(x)\,dx \right) - \hat{M} \tag{9a}$$

$$\hat{v} = \hat{\ell}^2 \partial_{\hat{x}}^2 v + \hat{\ell}\partial_{\hat{x}}\hat{\sigma}_a(\hat{M}) \tag{9b}$$

2

Parameter	Description	Value	Units	Ref	Notes
L	Domain length	134.6	μm	[4]	radii $27 \times 15\,\mu$m ellipse
h	Cytoplasmic "thickness"	9.5	μm	[4]	(area/circumference)
D_M	Myosin diffusivity	0.05	μm^2/s	[5]	
k_M^{on}	Myosin attachment rate	0.5	μm/s		Fit to get 30% bound myosin
k_M^{off}	Myosin detachment rate	0.12	1/s	[5]	
$M^{(\mathrm{Tot})}$	Maximum bound myosin density	–	#/μm		Scales out of equations
η	Cytoskeletal fluid viscosity	0.1	Pa·s		$100 \times$ water
γ	Myosin drag coefficient	10^{-3}	Pa·s/μm^2		$\ell = \sqrt{\eta/\gamma} = 10\,\mu$m [13]
σ_0	Stress coefficient and form	0.0042	Pa		Fit in Sec. 1.2.2
$\hat{\sigma}_a(\hat{M})$	Stress function of myosin	$\hat{M}$			Fit in Sec. 1.2.2

Table 1: Parameter values for myosin model. All of these parameters listed with a citation are lifted directly from the corresponding paper. Remaining parameters: the on rate k_M^{on} is chosen to give 30% bound myosin [5, Fig. S3]. Later this rate will change in the presence of CDC-42. We make an assumption about the fluid viscosity η, which then gives us the drag coefficient γ from $\ell = 10\,\mu$m [5]. The remaining parameters are fit in Section 1.2.2 from the wild-type data of [14].

and are controlled by the dimensionless parameters

$$\hat{\sigma}_0 = \left(\frac{\sigma_0/\sqrt{\eta\gamma}}{Lk_M^{\mathrm{off}}}\right) \qquad \hat{D}_M = \frac{D_M}{k_M^{\mathrm{off}}L^2} \qquad \hat{K}_M^{\mathrm{on}} = \frac{k_M^{\mathrm{on}}}{hk_M^{\mathrm{off}}} \qquad \hat{\ell} = \frac{\sqrt{\eta/\gamma}}{L}. \tag{10}$$

Recalling that $1/k_M^{\mathrm{off}}$ is the residence time, these dimensionless parameters can be understood in the following way:

1. $\hat{\sigma}_0$ is the fraction of the domain that active transport occurs on before a myosin molecule jumps off. To see this, note that residence time $\times$ the advective velocity $\sigma_0/\sqrt{\eta\gamma}$ is the amount of motion, which is normalized by the domain length.

2. $\hat{D}_M$ is the maximum fraction of the domain a molecule diffuses before it unbinds (in the extreme case when the gradient in the domain is $1/L$, the diffusive velocity is D_M/L).

3. $\hat{K}_M^{\mathrm{on}}$ is the ratio of the binding rate to unbinding rate when all the molecules are cytoplasmic. The uniform steady state of the model is given by $\hat{M}_0 = \hat{K}_M^{\mathrm{on}}/\left(1 + \hat{K}_M^{\mathrm{on}}\right)$.

4. $\hat{\ell}$ is the ratio of the hydrodynamic lengthscale to the domain length.

Prior to performing linear stability analysis, we need to first determine the function σ_a and the other parameters. We do this in the next section by fitting experimental data.

3

1.2.1 Parameter estimation

Table 1 lists the parameters for the myosin model. According to [4], the *C. elegans* embryo has a roughly ellipsoidal shape, with half-axis lengths $27 \times 15 \times 15$ μm. As such, our model will be a 27×15 ellipse, which has perimeter $L = 134.6$ μm. In our one-dimensional model, the cytoplasm has a "thickness" which is just the area of the ellipse 1272 μm^2 divided by the perimeter L, which gives $h = 9.5$ μm.

The next category of parameters relates to the myosin kinetics. The in-membrane diffusivity of myosin, as well as the detachment rate, have both been measured in [5]. For the attachment rate, it was estimated in [5, Fig. S3m] that roughly 30% of myosin is bound to the cortex in wild-type embryos. Recalling that the uniform steady state is $\hat{M}_0 = \hat{K}_M^{\mathrm{on}} / \left(1 + \hat{K}_M^{\mathrm{on}}\right)$, this gives $\hat{K}_M^{\mathrm{on}} = 0.43$, or $k_M^{\mathrm{on}} = 0.43 h k_M^{\mathrm{off}} = 0.5$ μm/s. The last parameter, the total amount of myosin, scales out of the equations. This is fortunate for us because it is difficult to think about a total amount over a cross-section.

For the fluid parameters, we assume that the viscosity of the cytoskeletal fluid on the cortex is 100 times water, which gives 0.1 Pa·s. The "hydrodynamic length scale" of $\ell = \sqrt{\eta/\gamma} = 10$ μm, measured in [13], then gives the myosin drag coefficient γ. But more important than either of these is the stress as a function of myosin concentration. We fit this from the wild-type data of [14] in the next section.

1.2.2 Inferring flow profile from experiments

Because we can measure the cortical velocity and myosin intensity, we can actually infer the function $\sigma_a(M)$ in dimensional units from the experimental data [14]. We in particular isolate the myosin intensity and flow speed during "late maintenance" phase in wild type embroys [14, Fig. 1B(bottom)], plotting the results in the top panels of Fig. 1. In the top left plot, we plot the myosin intensity, normalized so that the mean amount of bound myosin is 0.3, in accordance with wild-type measurements in [5, Fig. S3].

In the top right plot, we show the velocity in μm/min. In both cases, the data are plotted on $\hat{x} \in [0.25, 0.75]$, which corresponds to half of the embryo (one of the lines going from anterior to posterior end). We then periodically extend this data so that we fill the whole circumference $\hat{x} \in [0, 1]$; these are the blue lines in Fig. 1. Finally, to remove the noise from our measurements (e.g., the strange dips in the myosin concentration at the anteior and posterior pole), we fit the
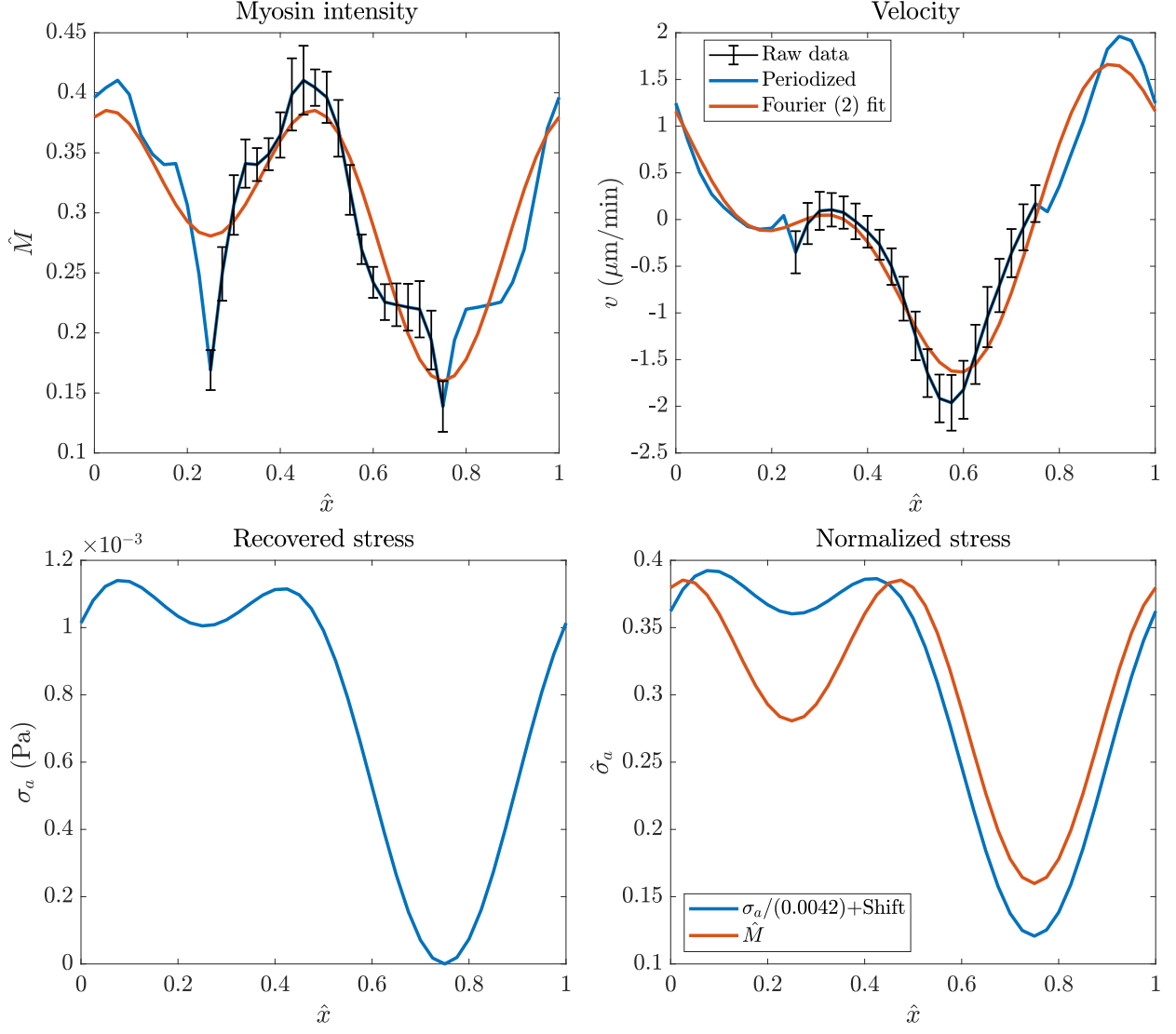
Figure 1: Extracting the velocity profile and active stress from wild-type embryos. Top: the experimental data for myosin intensity (left) and velocity in μm/min (right). We show the raw data in black (which goes from anterior to posterior), the periodized version in blue, and a two-term (three terms if we include the constant) Fourier series representation in red. Bottom left: the recovered stress profile $\sigma_a(\hat{x})$ in dimensional units. Bottom right: comparing the recovered stress to the myosin intensity, after normalizing by $\sigma_0 = 0.0011$ Pa. It is clear that $\hat{\sigma}_a = \hat{M}$ is a reasonable approximation.

periodized version with a two-term (+constant) Fourier representation, which gives the red lines in Fig. 1.

To extract the stress profile from the smoothed velocity and myosin intensity, we consider a hybrid dimensional form of (7b)

$$\gamma v - \frac{\eta}{L^2} \partial_{\hat{x}}^2 v = \frac{1}{L} \partial_{\hat{x}} \sigma_a(M).$$

Let the Fourier series representation for $v(\hat{x}) = \sum_k \tilde{v}(k) \exp(2\pi i k \hat{x})$, and likewise for $\hat{\sigma}_a$. Then, in Fourier space, the solution for σ_a is given by

$$\sigma_a(k) = \frac{\gamma + \eta/L^2 (2\pi k)^2}{2\pi i k/L} \tilde{v}(k). \tag{11}$$

The $k = 0$ mode is undefined because σ_a only appears differentiated; we therefore set it such that the real space stress has a minimum value of zero.

We plug the parameters from Table 1 into (11) and show the resulting real space stress in the bottom left panel of Fig. 1. This is the dimensional stress σ_a. In the right panel of Fig. 1, we normalize and shift the stress so that it has the same mean and range as the myosin profile $\hat{M}$. Obtaining the same range allows us to read off the constant $\sigma_0 = 4.2 \times 10^{-3}$ Pa that controls the magnitude of the advective flows. In particular, the dimensionless parameter $\hat{\sigma}_0$ defined in (10) is seen to be equal to

$$\hat{\sigma}_0 = \left(\frac{\sigma_0/\sqrt{\eta\gamma}}{L k_M^{\text{off}}} \right) = 0.026. \tag{12}$$

In additiom, the bottom right panel of Fig. 1, also shows that we can roughly set

$$\hat{\sigma}_a = \hat{M} \tag{13}$$

as a good approximation to the stress. The function itself is ambiguous, since $\hat{M} = 0.3$ defines two different values of the stress depending on the side of the domain, but $\hat{\sigma}_a = \hat{M}$ appears to be a good approximation.

We confirm this in Fig. 2, where we repeat the velocity fitting procedure in *arx-2* (RNAi) embryos, which lack branched actin and consequently have a simpler velocity profile. To compute the myosin profile, we assume that the experimentally-measured intensity can be converted to the dimensionless concentration $\hat{M}$ via the same factor (0.21) as wild-type embryos. Consequently, the myosin profile we obtain is in the top left of Fig. 2. The velocity is shown in the top right panel, and we extract the stress profile in the bottom left in exactly the same way as in wild-type. Then, to compute normalize stress we divide out by $\hat{\sigma}_0 = 4.2 \times 10^{-3}$ Pa (obtained from wild-type).
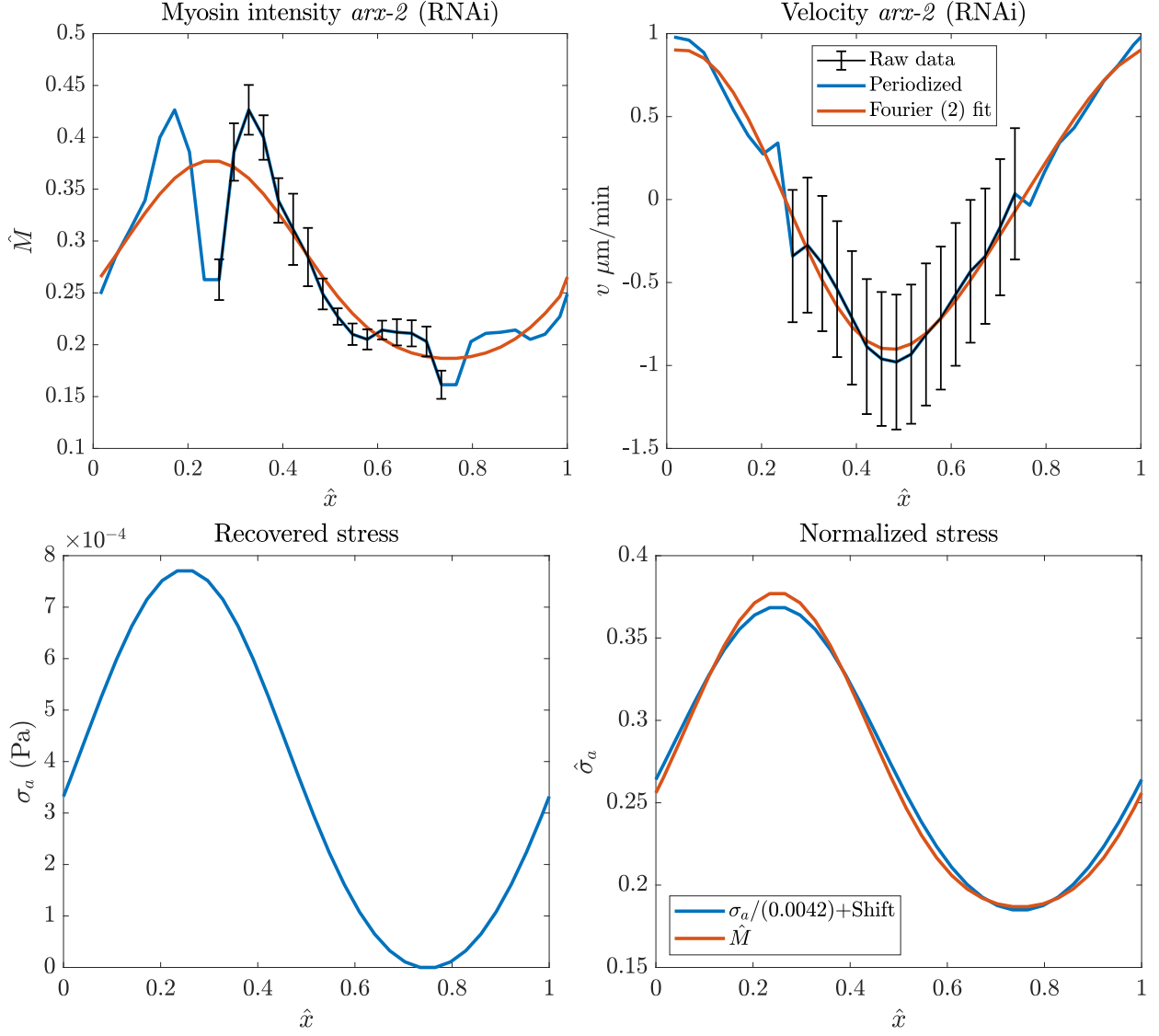
Figure 2: Same plot as Fig. 1, but in *arx-2* (RNAi) embryos. In the bottom right plot, we normalize by $\sigma_0 = 1.1 \times 10^{-3}$ Pa. This makes the stress (when shifted by an arbitrary constant) roughly the same as the myosin profile (also normalized so its maximum is 1).

The normalized stress, when shifted by an arbitrary constant, lines up almost perfectly with the smoothed myosin profile, demonstrating that our rough approach from wild-type embryos extends to other embryos as well. Thus, this section gives us $\sigma_a = \left(4.2 \times 10^{-3}\right) \hat{M}$.

1.2.3 Linear stability analysis

Now that all the parameters are known, we can perform linear stability analysis to see if the system could spontaneously polarize. The uniform steady state is $\hat{M}_0 = \hat{K}_M^{\text{on}}/\left(1 + \hat{K}_M^{\text{on}}\right)$. We consider a perturbation around that state $\hat{M} = \hat{M}_0 + \delta\hat{M}$, where $\delta\hat{M} = \delta\hat{M}_0 e^{\lambda(k)\hat{t}+2\pi ik\hat{x}}$. Plugging this into (9b), we get the velocity [2, Eq. (11)]

$$\hat{v} = \frac{2\pi ik\hat{\ell}\hat{\sigma}_a'(\hat{M}_0)}{1 + \left(2\pi k\hat{\ell}\right)^2}\hat{\delta}M.$$
(14)

Substituting this velocity into (9a), and considering only the first order terms, we get the following equation for the eigenvalues

$$\lambda(k) = \frac{4\pi^2 k^2 \hat{\ell}\hat{M}_0\hat{\sigma}_0\hat{\sigma}_a'(\hat{M}_0)}{1 + 4\pi^2 k^2 \hat{\ell}^2} - \hat{D}_M 4\pi^2 k^2 - 1$$
(15)

Using the parameters we have obtained, we have the following values for the dimensionless groups

$$\hat{D}_M = 2.3 \times 10^{-5} \qquad \hat{M}_0 \approx 0.3 \qquad \hat{\sigma}_a' = 1 \qquad \hat{\ell} \approx 0.07$$
(16)

This gives the dispersion relation shown in Fig. 3 for different values of $\hat{\sigma}_0$. We observe strong flow coupling required for instability; with $\hat{\sigma}_0 = 0.2$ (flow transports myosins around 20% of the cell before they come off), we still do not see any instability. Considering that we already have seen wild-type embryos have $\sigma_0 \approx 0.004$, it is clear that myosin cannot self-polarize in the zygote.

Importantly, the large value of σ_0 needed for instability is a consequence of the -1 in the dispersion relation (15), which comes from the unbinding kinetics. Thus, unbinding makes it *harder* to destabilize the uniform steady state. Indeed, without the -1, the instability occurs at $\hat{\sigma}_0 \approx 10^{-3}$, which is pretty weak coupling to the flow. When we account for unbinding, diffusion becomes so small as to be irrelevant, as for the $k = 1$ mode the coefficient in (15) is $\hat{D}_M 4\pi^2 \approx 10^{-3}$. **Thus, the real balance here (to generate the instability) is not between advection and diffusion, but between advection and *unbinding*.** Specifically, the advective flow must be strong enough to overcome the increase in unbinding that happens in areas enriched in myosin.
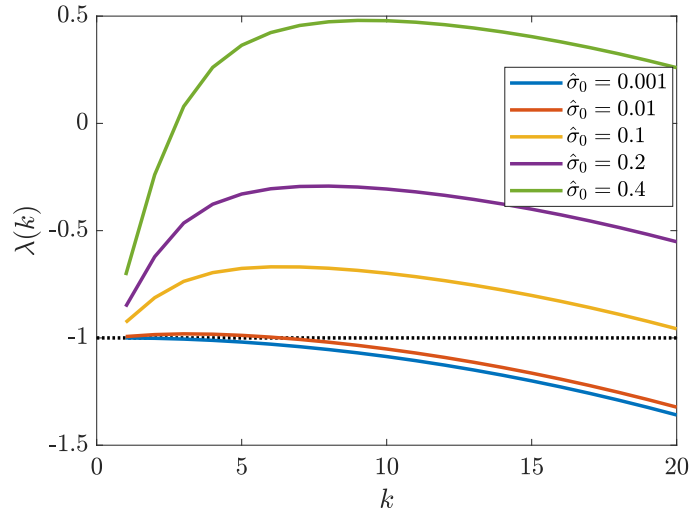
8

Figure 3: Dispersion relation (15) for myosin for different values of $\hat{\sigma}_0$. Positive eigenvalues indicate instability of the steady state. Dotted black line at $\lambda = -1$ reflects the axis of instability *without* unbinding kinetics.

2 PAR-3 as the anchor for asymmetries

We are motivated first by the experimental observations that asymmetries in the PAR proteins are stable once set up, even in the absence of contractility. This experimental observation tells us that there is an intrinsic bistability in the biochemical circuit, which switches from a uniform state to a polarized state. In later sections, the switch will occur under the influence of actomyosin flows, while in this section the initial conditions will be the only way to switch the steady profiles.

Unlike in budding yeast cells [11], there is no experimental evidence that *C. elegans* cells can spontaneously polarize, which means that the system is truly bistable. Traditionally, it has been speculated that the bistability comes from mutual inhibition of the aPAR and pPAR proteins [6, 16]. But translating this idea into equations becomes much harder than might be expected! Indeed, ODEs based on first-order mass action kinetics of aPAR-pPAR inhibition *do not* yield bistable dynamics under any choice of parameters [3]. Attempts to overcome this have used stoichiometric coefficients for the biochemical equations that guarantee bistability [4, 5] or included actomyosin flows designed to transport the aPARs [15]. Both of these approaches are grounded more in intuition than in biological evidence, as there is no reason to doubt mass action kinetics, and recent experiments have shown that both aPARs and pPARs are transported by myosin [7].

Recent experimental observations about PAR-3 provide a potential way out of this conundrum.

Indeed, it was recently shown that PAR-3 asymmetries are stable even in the absence of its posterior inhibitor PAR-1, which suggest that the dynamics of PAR-3 *by itself* are intrinsically bistable [8]. Experimental evidence has shown that the bistability occurs via a mechanism in which membrane-bound PAR-3 recruits additional cytoplasmic monomers to the membrane. One goal of this section is to translate these observations into equations which demonstrate how PAR-3 can set up and maintain an asymmetry in the absence of posterior inhibition. We then incorporate posterior PAR proteins and show how their inclusion modifies the dynamics of PAR-3, potentially shifting the boundary between the two protein domains.

2.1 Basic equations and framework for PAR-3

We first formulate our model of PAR-3 dynamics, which is based loosely on that of Lang and Munro [10]. The key property of PAR-3 that makes it different from other proteins is its ability to form *oligomers* on the membrane. Unlike monomers, these oligomers do not diffuse in the membrane, and are not found in high concentrations in the cytoplasm. Based on these experimental observations, we will consider a model in which there are two species of PAR-3,

1. Monomeric PAR-3, which can be found in cytoplasmic form (A_{cyto}) or membrane bound (A_1) form.

2. Oligomerized PAR-3 (A_n) which is only found on the membrane and can neither diffuse nor become unbound. These assumptions are approximations based on the experimental observations in [8, Fig. 3K], which show that the dissociation rate constant for dimers in trimers is 5–10 times smaller than that for monomers, and also the experimental observation that PAR-3 only binds to the membrane in monomer form [8].

Given these assumptions, the model equations in dimensional form are as follows

$$\partial_t A_1 = D_A \partial_x^2 A_1 + \left(k_A^{\text{on}} + k_A^+ f_A^+ (A_1, A_n)\right) A_{\text{cyto}} + 2k_A^{\text{dp}} A_n - 2k_A^{\text{p}} A_1^2 - k_A^{\text{off}} A_1 \tag{17a}$$

$$\partial_t A_n = k_A^{\text{p}} A_1^2 - k_A^{\text{dp}} A_n \tag{17b}$$

$$A_{\text{cyto}} = \frac{1}{hL} \left(A^{(\text{Tot})} L - \int_0^L \left(A_1(x) + 2A_n(x) \right) dx \right) \tag{17c}$$

A complete list of parameters with units and values is given in Table **??**, but it will be helpful to point out the important ones in our model. First, the feedback strength k_A^+, which has units of length^2/time, gives the rate at which cytoplasmic PAR-3 is recruited to the membrane. It is

multiplied by the flux function f_A^+, which gives the strength of recruitment (in units of inverse length; this could be as simple as $f_A^+(x, y) = x + 2y$). The overall on rate is proportional to the cytoplasmic concentration, which is defined in (17c). There $A^{(\mathrm{Tot})}$ expresses the density of bound PAR-3 when all molecules are bound to the membrane (units 1/length). Subtracting the amount of bound PAR-3 and dividing by the membrane area gives the cytoplasmic concentration in units of 1/area.

2.2 Dimensionless form

A sensible timescale for the system is the time a given PAR-3 molecule spends on the membrane. Because about 80% of the bound PAR-3 molecules are in oligomer form, and since the depolymerization reaction is much slower than the unbinding reaction, we nondimensionalize time by $1/k_A^{\mathrm{dp}}$. This gives the dimensionless (hatted) variables defined by

$$ x = \hat{x}L \qquad t = \hat{t}/k_A^{\mathrm{dp}} \qquad A = \hat{A}A^{(\mathrm{Tot})}. $$

Substituting into (17) gives the rewritten dynamics

$$ \partial_{\hat{t}} \hat{A}_1 = \hat{D}_A \partial_{\hat{x}}^2 A_1 + \hat{K}_A^{\mathrm{on}} \left(1 + \hat{K}_A^+ \hat{F}_A^+ (\hat{A}_1, \hat{A}_n) \right) \left(1 - \int_0^1 \hat{A}(x) \, d\hat{x} \right) $$

$$ + 2\hat{K}_A^{\mathrm{dp}} \hat{A}_n - 2\hat{K}_A^{\mathrm{p}} \hat{A}_1^{\,2} - \hat{K}_A^{\mathrm{off}} \hat{A}_1 \tag{18a} $$

$$ \partial_{\hat{t}} \hat{A}_n = \hat{K}_A^{\mathrm{p}} \hat{A}_1^{\,2} - \hat{K}_A^{\mathrm{dp}} \hat{A}_n \tag{18b} $$

$$ \hat{D}_A = \frac{D_A}{L^2 k_A^{\mathrm{dp}}}, \quad \hat{K}_A^{\mathrm{on}} = \frac{k_A^{\mathrm{on}}}{k_A^{\mathrm{dp}} h}, \quad \hat{K}_A^+ = \frac{k_A^+ A^{(\mathrm{Tot})}}{k_A^{\mathrm{on}}}, \quad \hat{K}_A^{\mathrm{off}} = \frac{k_A^{\mathrm{off}}}{k_A^{\mathrm{dp}}}, \tag{18c} $$

$$ \hat{K}_A^{\mathrm{p}} = \frac{k_A^{\mathrm{p}} A^{(\mathrm{Tot})}}{k_A^{\mathrm{dp}}}, \quad \hat{K}_A^{\mathrm{dp}} = 1, \quad \hat{F}_A^+(\hat{A}_1, \hat{A}_n) = \frac{f_A^+(A_1, A_n)}{A^{(\mathrm{Tot})}} $$

and we have used the convenient shorthand $A = A_1 + 2A_n$ and likewise for the hatted variables.

2.3 Parameters

Recent experimental measurements [8] give accurate measurements for three of the parameters: the diffusion coefficient D_A, the detachment rate of monomers k_A^{off}, and the depolymerization rate k_A^{dp}. The values of these parameters are summarized in Table **??**, and determine the dimensionless parameters $\hat{D}_A$ and $\hat{K}_A^{\mathrm{off}}$. We determine $\hat{K}_A^{\mathrm{on}}$, $\hat{K}_A^{\mathrm{p}}$, $\hat{K}_A^+$, and the form of the feedback function via a systematic fitting procedure as detailed next.

2.3.1 Fitting the polymerization rate

The first parameter we need to fit the polymerization rate is the percentage of PAR-3 bound to the membrane in the uniform state. The uniform state can be realized by considering mutants which lack a functional sperm cue and thus do not polarize [8, Fig. S1]. These mutants show a peak PAR-3 concentration in late interphase; late maintenance phase then gives a bound concentration that is roughly 50% of this peak. We will assume that almost all of the PAR-3 is bound in late interphase, so that the uniform state is at $\hat{A}_u := \hat{A}_1 + 2\hat{A}_n \approx 0.5$. The observation that these embryos do not polarize implies that the uniform state is stable, and the estimate for the percentage of bound protein is similar to that obtained for PAR-2 at the end of maintenance phase in [5, Fig. S3].

When there is no posterior inhibitor, the concentration of bound PAR-3 during late maintenance phase in the anterior is roughly $\hat{A}_a = 1.2u \approx 0.6$ (this comes from comparing flourescence in PAR-1 mutant and spd-5 mutant embryos shown in Figs. 2 and S1 of [8]). In PAR-1 mutants, the concentration in the posterior is then roughly 10% of the anterior, or $\hat{A}_p = 0.06$.

These measurements allow us firstly to determine the relative polymerization rate $\hat{K}_A^{\mathrm{p}}$. The distribution of oligomer sizes in PAR-1 mutant embryos was measured in [8] on both the anterior and posterior side. There it was shown that the distribution is roughly exponential, so that a_n, the number of size n is $a_n = \alpha^{n-1}a_1$. This implies that the fraction in monomer form is $(1-\alpha)^2$. Using the measurements in [8], we have $\alpha = 0.42$ on the posterior side (30% in monomer form), and $\alpha = 0.73$ on the anterior side (10% in monomer form) by solving (18b) at steady state to obtain the relationship

$$\frac{\hat{A}_1}{\hat{A}} = \frac{1}{4\hat{A}\hat{K}_A^{\mathrm{p}}}\left(-1 + \sqrt{1 + 8\hat{A}\hat{K}_A^{\mathrm{p}}}\right). \tag{19}$$

We then insist that $\hat{A} = 0.6 \to \hat{A}_1 = 0.06$ and solve for $\hat{K}_A^{\mathrm{p}}$, which gives $\hat{K}_A^{\mathrm{p}} = 75$. The corresponding value on the posterior side is $\hat{A} = 0.06$ and $\hat{A}_1 = 0.017$, which is roughly 28% of the protein in monomer form, matching the experimental observation.

2.3.2 The form of the feedback strength – linear feedback models

Before we get into fitting the feedback parameters, it is important to consider the nature of the feedback model. Our model is based strongly on that of Lang and Munro [10], who used the linear feedback model
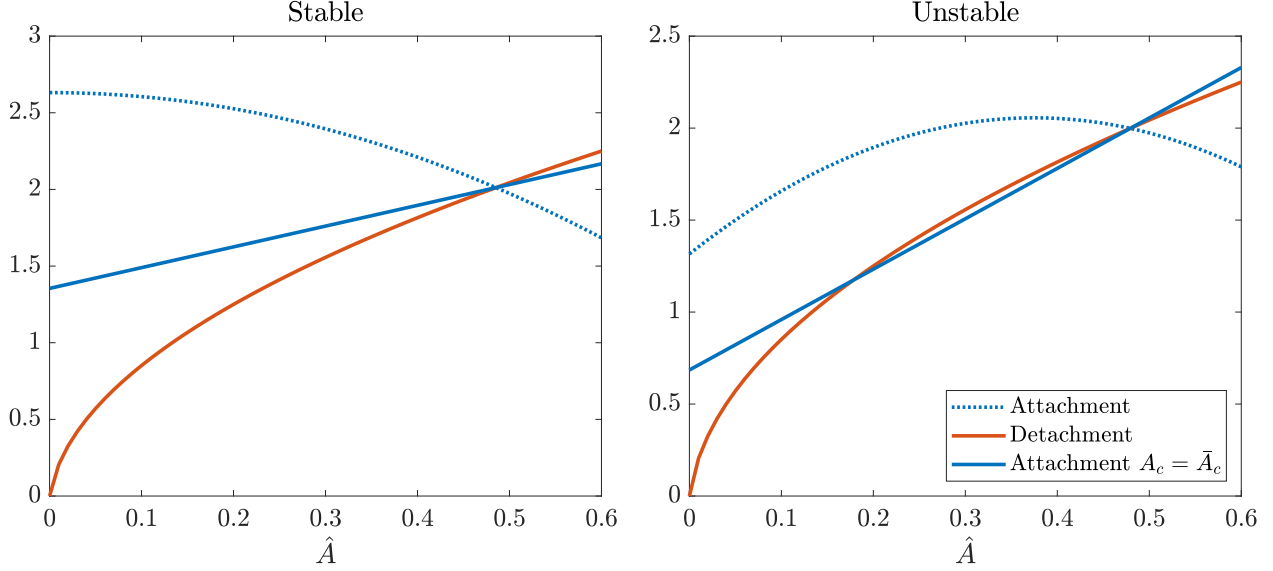
$$f_A^+(A_1, A_n) = A_1 + 2A_n = A.$$

Figure 4: Flux plane analysis for linear feedback in the stable (left) and unstable (right) case. The stability analysis is determined by how the attachment rate (solid blue line, with constant cytoplasmic concentration) compares to the detachment rate (red) near the steady state.

To analyze the characteristics of this model, we consider two representative examples in Fig. 4, where we look at the attachment and detachment fluxes as a function of $\hat{A}$. The detachment flux is simply $\hat{K}_A^{\text{off}} \hat{A}_1$, and is therefore set by the red line. The attachment flux varies depending on the model considered. If we consider a uniform state, then the cytoplasmic concentration is simply $1 - \hat{A}$, and there is a single uniform steady state (intersection of dotted blue and red lines). In polarized states, the concentration is not necessarily uniform, and so we analyze the stability of the steady state by taking the cytoplasmic concentration as constant. This results in the darker blue line in Fig. 4. There we see that the linear feedback model admits only two possibilities: a stable uniform state (when feedback is small relative to the on-rate), and an unstable uniform state which leads to spontaneous polarization (when the feedback is larger). This contradicts our experimental observation of *bistability*.

For the uniform steady state to be stable, the attachment rate at constant cytoplasmic concentration has to be smaller than the detachment rate, as shown in the left panel of Fig. 4. At the same time, for bistability, the attachment flux at constant cytoplasmic concentration has to intersect the detachment curve three times (two stable fixed points and one unstable fixed point in between). A simple way to accomplish this is by setting

$$f_A^+(A_1, A_n) = \min\left(A_1 + 2A_n, A_{\text{sat}}\right) \rightarrow F_A^+(\hat{A}_1, \hat{A}_n) = \min\left(\hat{A}_1 + 2\hat{A}_n, \hat{A}_{\text{sat}}\right). \tag{20}$$
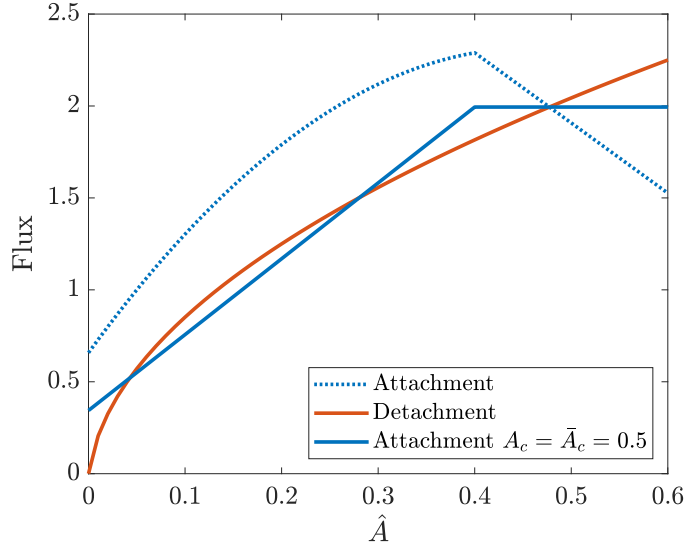
13

Figure 5: Flux plane analysis for capped linear feedback in the bistable case ($\hat{K}_A^+ = 12$ and $k_A^{\mathrm{on}} = 0.5$ μm/s). The stability analysis is determined by how the attachment rate (solid blue line, with constant cytoplasmic concentration) compares to the detachment rate (red) near the steady state.

The uniform steady state is stable if $\hat{A}_{\mathrm{sat}} < u = 0.5$, which provides one constraint on the saturation. The second constraint comes from bistability; the system is only locally bistable at fixed cytoplasmic concentration when $\hat{A}_{\mathrm{sat}}$ is close to the uniform state (if $\hat{A}_{\mathrm{sat}}$ is too small the feedback becomes essentially constant and cannot generate bistability). Based on these considerations, we set $\hat{A}_{\mathrm{sat}} = 0.4$.

Once $\hat{A}_{\mathrm{sat}} = 0.4$ is set, there are two unknown parameters, the on rate k_A^{on} and the strength of the feedback $\hat{K}_A^+$. In Fig. 5, we set these two parameters so that, at the cytoplasmic concentration of the uniform state, the system has a second steady state at roughly 10% of the uniform state. The bistable solution exists for a narrow range of cytoplasmic concentration – when the cytoplasmic concentration is too small or too large, the attachment flux only crosses the detachment flux once, which means that there is no stable state for these cytoplasmic concentrations. Suppose we have the cytoplasmic concentration A_c, and let $\hat{A}_1$ and $\hat{A}_2$ be the two stable states at this concentration. Then in the absence of diffusion, if the equation

$$(1 - y)\hat{A}_1(A_c) + y\hat{A}_2(A_c) = 1 - A_c \tag{21}$$

has a solution, then y defines the boundary position. Otherwise, there will be a uniform state.

This completes our parameter selection for the PAR-3 model. The parameters we use going forward are summarized in Table 2.

Parameter	Description	Value	Units	Ref	Notes
D_A	Monomeric PAR-3 diffusivity	0.1	$\mu m^2/s$	[8]	
k_A^{on}	Monomeric PAR-3 attachment rate	0.5	$\mu m/s$		Fit for uniform state $\hat{A} = 0.5$
k_A^{off}	Monomeric PAR-3 detachment rate	3	$1/s$	[8]	(Fig. 3K)
k_A^{dp}	PAR-3 depolymerization rate	0.08	$1/s$	[8]	(Fig. 4E)
$\hat{K}_A^{\text{p}}$	PAR-3 polymerization rate	75			Fit for correct % monomers [8]
$\hat{K}_A^{+}$	PAR-3 self recruitment rate	12			Fit for bistability
F_A^{+}	PAR-3 feedback function	$\min\left(\hat{A}, 0.4\right)$		[10]	Modified for stable uniform state
$A^{(\text{Tot})}$	Maximum bound PAR-3 density	–	$\#/\mu m$		Contained in other unknowns

Table 2: Additional parameter values for the PAR-3 model.

2.4 Results for bistable PAR-3 model

2.4.1 Steady states

We now look at the steady states of the PAR-3 model with the parameters in Table 2. Figure 6 shows what happens when we run from $\hat{t} = 0$ to $\hat{t} = 500$, which achieves the steady state. In the top left plot, we see that the uniform steady state is stable, as expected from the stability diagram. But when the perturbation to the uniform state is too large, or when we introduce an asymmetry into the system by depleting PAR-3 in part of the domain, we see bistable dynamics where the small part gravitates to one steady state, while the larger end goes to another. In the bistable region, we observe a posterior concentration which is always roughly 10% of the anterior concentration, as desired (the exact number at steady state is $0.046/0.49 = 9.3\%$.

In the case when we deplete PAR-3 in part of the domain, the bistable behavior only happens when the initial domain size is sufficiently large. Figure 6 demonstrates this in the bottom row, where we consider initial domains of PAR-3 enrichment of 0.9 (bottom left) and 0.5 (bottom right). We find that when the initial PAR-3 domain of enrichment is larger than 50% of the domain, the system tends to the bistable state, with about 95% of the domain enriched in PAR-3 and 5% at the lower state. When the initial domain of PAR-3 enrichment is too low, however, we find that the flux into the depleted regions is too large, and those regions tend to surpass the smaller uniform steady state and be attracted to the larger one. The higher flux happens because of a larger cytoplasmic concentration (which could result from the initial condition, or from unbinding from the enriched domain if we try to deplete the cytoplasm initially). In any case, the conclusion of Fig. 6 is that there is a uniform steady state, which is the attractor when most of the PAR-3 is initially in the
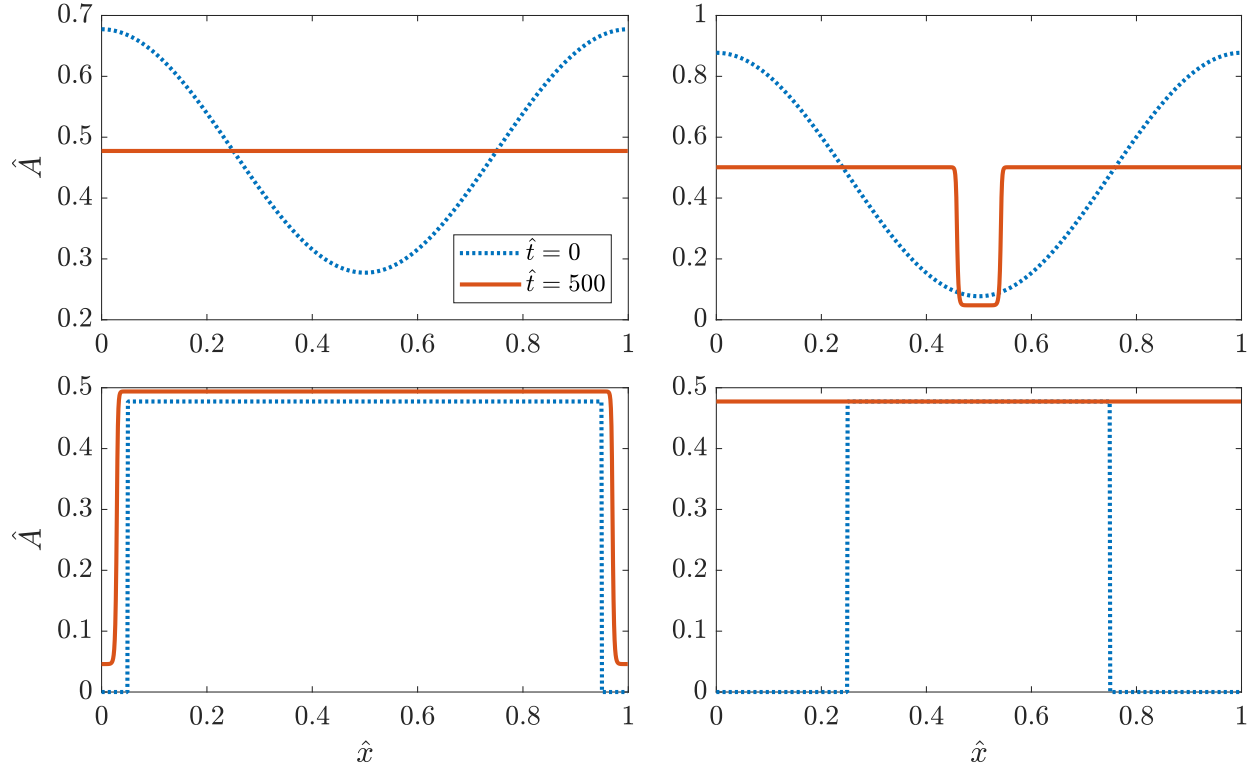
Figure 6: Simulating the PAR-3 feedback model with the parameters in Table 2. The initial conditions are shown in dotted blue, and the distribution at $\hat{t} = 500$ ($\hat{t} = 1$ corresponds to 12.5 seconds of real time) is in red. In the top row, we make a continuous perturbation from the uniform state, finding that large enough perturbations induce bistability. In the bottom row, we start with a peaked initial profile of large and small size, finding that only larger (than 0.5) initial profiles can lead to bistability.
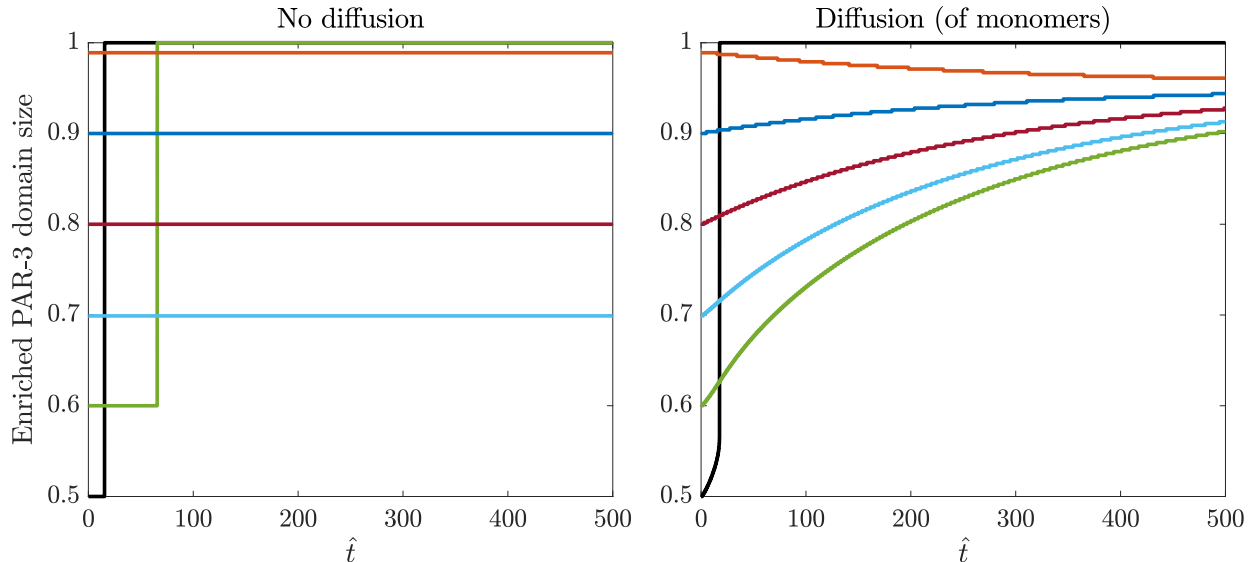
Figure 7: Size of PAR-3 domain over time without (left) and with (right) diffusion of monomeric PAR-3. Without diffusion, any boundary position with 70% or more enriched PAR-3 is stable, because there exists a solution to (21) where the on rate balances the off rate in both the enriched and depleted regions. When we introduce diffusion, there is an additional constraint in the boundary layer which specifies a unique boundary position.

cytoplasm, and a bistable state, which is an attractor when the cytoplasmic concentration is around 0.5 (50% of protein in the cytoplasm).

2.4.2 Position of boundary and approach to steady state

Let us now try to understand the position of the boundary. In Fig. 7, we plot the size of the enriched PAR-3 domain over time for various initial boundary positions. We start without diffusion, observing that, for sizes of the enriched PAR-3 domain 0.5 or larger, the cytoplasmic concentration is sufficiently low for a bistable solution to exist (left panel of Fig. 7). When the PAR-3 domain is initially too small, the cytoplasmic concentration at steady state would be too high for bistability, and so the uniform state is the only stable one. If the bistable solution exists, then the boundary position does not move in time; any domain size 0.5 or larger appears to be stable.

This is not the case when we add diffusion into the model, which provides an additional constraint. In this case, the right panel of Fig. 7 shows that there is a *unique* boundary position that the system tends to, when the diffusive flux in the *boundary layer* balances the net unbinding and binding fluxes. Indeed, when we turn on diffusion, there is diffusion of monomers away from the
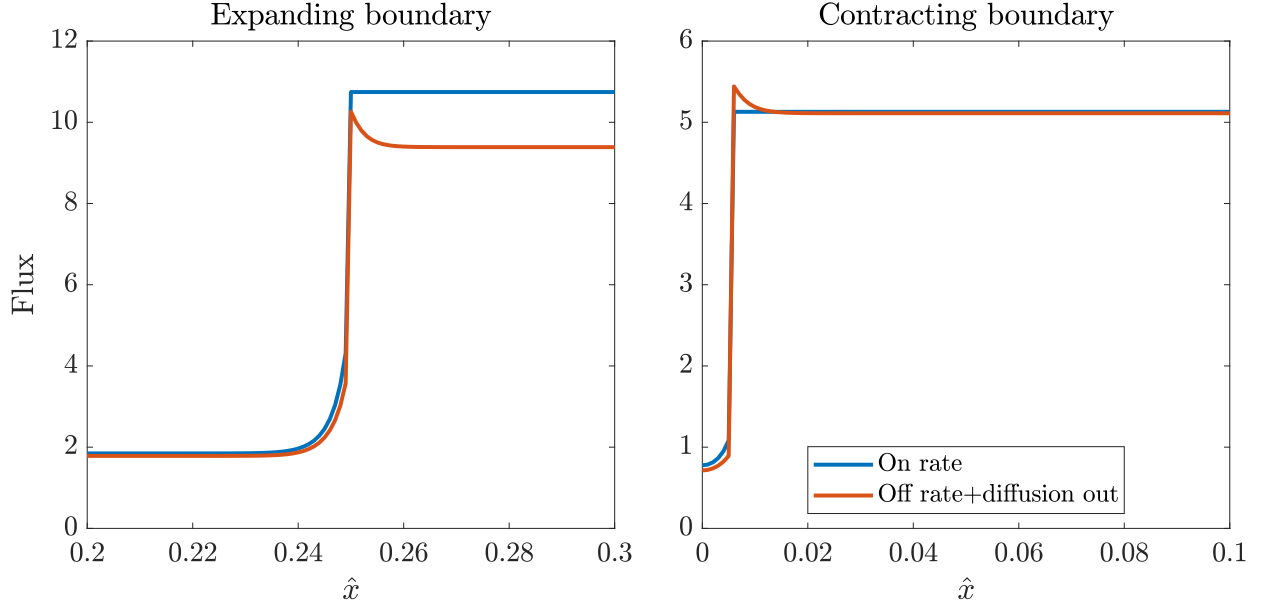
Figure 8: Local depletion by diffusion and consequent expansion/contraction of boundary. These figures show the positive fluxes due to binding (blue) and the negative fluxes due to diffusion and unbinding (red). When the boundary is narrow (left figure), the binding rate is higher due to enriched cytoplasm, and the boundary expands. On the other hand, when the boundary is wider (right figure), the binding rate is locally lower than the off rate + diffusion (note diffusion makes the difference in this case), and the boundary contracts.

enrichment zone, and consequently local depletion of monomers at the edge of the enrichment zone (oligomers are not depleted, so the on flux is basically unchanged). There is then an imbalance of flux where the flux from binding is larger than the unbinding flux at the edge of the enrichment zone. If the on rate dominates diffusion (this is the case when the cytoplasm is enriched), then the boundary will tend to expand. On the other hand, if diffusive fluxes are sufficiently large (cytoplasmic depletion or larger zone of enrichment), then the boundary will contract if diffusive flux outwards overcomes the increased local binding. Figure 8 shows examples of this.

Another observation from Fig. 8 is the *rate* at which the boundary shifts to the steady state. Because the rate of expansion/contraction is controlled by diffusion of monomers, and because the dimensionless diffusivity $\hat{D}_A \approx 7 \times 10^{-5}$, the movement of the boundary is quite slow. Indeed, most embryos are in maintenance phase for about 10 minutes, which corresponds to $\hat{t} = 48$. During this time, the movement of the boundary is at most 5% of the perimeter, or about 10% of the embryo length. Similar arguments to this were made in [10] to justify the possibility that the uniform steady state is unstable, and that the polarized PAR-3 state (in which PAR-3 is stably enriched on

Parameter	Description	Value	Units	Ref	Notes
D_P	PAR-2 diffusivity	0.15	$\mu\text{m}^2/\text{s}$	[4]	
k_P^{on}	PAR-2 attachment rate	0.6	$\mu\text{m}/\text{s}$		90% bound PAR-2 no inhibition
k_P^{off}	PAR-2 detachment rate	7.3×10^{-3}	$1/\text{s}$	[4]	
$\hat{R}_{\text{AP}}$	Rate of P inhibition by A	100			Fit small P in anterior
$\hat{R}_{\text{PA}}$	Rate of A inhibition by P	0.5			Fit boundary position
$P^{(\text{Tot})}$	Maximum bound PAR-2 density	$-$	$\#/\mu\text{m}$		Included in $\hat{R}_{\text{PA}}$

Table 3: Additional parameter values for the PAR-3 model when PAR-2 is also included.

one half of the embryo) [8] might be a transient state that transitions to a large peak if we were to wait long enough. Here we propose that the polarized state of PAR-3 in the absence of PAR-1 is a result of the initial sperm cue, and that, if given long enough, the position of the boundary would relax towards the posterior side.

2.5   PAR-3 / PAR-2 bistable model

Let's now add posterior PARs (a single variable P which represents the PAR-1/PAR-2 conglomerate) to the model of PAR-3, so that the equations are

$$\partial_t A_1 = D_A \partial_x^2 A_1 + \left(k_A^{\text{on}} + k_A^+ f_A^+ \left(A_1, A_n \right) \right) A_{\text{cyto}} - k_A^{\text{off}} A_1 - 2k_A^{\text{p}} A_1^2 + 2k_A^{\text{dp}} A_n, \tag{22a}$$

$$\partial_t A_n = k_A^{\text{p}} A_1^2 - k_A^{\text{dp}} A_n - r_{\text{PA}} A_n P \tag{22b}$$

$$\partial_t P = D_P \partial_x^2 P + k_P^{\text{on}} P_{\text{cyto}} - k_P^{\text{off}} P - r_{\text{AP}} P \left(A_1 + 2A_n \right), \tag{22c}$$

Here we have assumed that PAR-3 inhibits PAR-2 (by activating PKC-3, which is not included here for simplicity) [9]. It is possible here to model PAR-2 in terms of both dimers and monomers [1]; however, because PKC-3 acts on both monomers and dimers, the two are really only separated by kinetics of dimerization.

Repeating our non-dimensionalization from (18), the dimensionless form of the equations (22)

is

$$\partial_{\hat{t}}\hat{A}_1 = \hat{D}_A\partial_{\hat{x}}^2 A_1 + \hat{K}_A^{\text{on}}\left(1 + \hat{K}_A^+ F_A^+\left(\hat{A}_1, 2\hat{A}_n\right)\right)\left(1 - \int_0^1 \hat{A}(x)\,d\hat{x}\right)$$

$$+ 2\hat{K}_A^{\text{dp}}\hat{A}_n - 2\hat{K}_A^{\text{p}}\hat{A}_1^2 - \hat{K}_A^{\text{off}}\hat{A}_1 \tag{23a}$$

$$\partial_{\hat{t}}\hat{A}_n = \hat{K}_A^{\text{p}}\hat{A}_1^2 - \hat{K}_A^{\text{dp}}\left(1 + \hat{R}_{\text{PA}}\hat{P}\right)\hat{A}_n \tag{23b}$$

$$\partial_{\hat{t}}\hat{P} = \hat{D}_P\partial_{\hat{x}}^2 \hat{P} + \hat{K}_P^{\text{on}}\left(1 - \int_0^1 \hat{P}(\hat{x})\,d\hat{x}\right) - \hat{K}_P^{\text{off}}\left(1 + \hat{R}_{\text{AP}}\hat{A}\right)\hat{P} \tag{23c}$$

$$\hat{R}_{\text{PA}} = \frac{r_{\text{PA}}P^{(\text{Tot})}}{k_A^{\text{dp}}}, \quad \hat{R}_{\text{AP}} = \frac{r_{\text{AP}}A^{(\text{Tot})}}{k_P^{\text{off}}}, \quad \hat{D}_P = \frac{D_P}{L^2 k_A^{\text{dp}}}, \quad \hat{K}_P^{\text{on}} = \frac{k_P^{\text{on}}}{k_A^{\text{dp}}h}, \quad \hat{K}_P^{\text{off}} = \frac{k_P^{\text{off}}}{k_A^{\text{dp}}} \tag{23d}$$

The additional dimensionless parameters are in (23d). All other dimensionless parameters have already been defined and determined in Section 2.3.

2.5.1 Parameters

There are therefore five parameters that are unknown in the model (23). The diffusion and dissociation rates of PAR-2 have been measured in [4], and are reported in Table 3. The mutual inhibition parameters and on rate k_P^{on} can be fit with the following three experimental observations:

1. In embryos without myosin flows, the level of PAR-2 at the anterior is no more than 5% of the posterior level [5, Fig. 2c]. This sets $\hat{R}_{\text{AP}} \gg 1$. We use $\hat{R}_{\text{AP}} = 100$ for strong inhibition.

2. In embryos without myosin flows, roughly 25–30% of the available PAR-2 is bound at steady state [5, Fig. S3]. Because the PAR-2 domain is only 25–30% of the embryo, the on rate in the absence of inhibition must be such that almost all of the cytoplasmic protein is bound. This sets $k_P^{\text{on}} = 0.6\ \mu\text{m/s}$ (90% bound no inhibition).

3. In embryos without myosin flows, the steady state boundary is at 70–75% PAR-3 enrichment [17, Fig. 5B]. This sets $\hat{R}_{\text{PA}} = 0.5$.

We try to tune the inhibition parameter in Fig. 9 to achieve the correct boundary position at steady state. When there is no inhibition (left plot), PAR-3 develops its bistable state naturally, and we can tune the distribution of PAR-2 by changing $\hat{R}_{\text{AP}}$ and k_P^{on} (not shown). Introducing nonzero $\hat{R}_{\text{PA}}$ then causes the boundary to shift, as depletion of PAR-2 in the interior leads to more cytoplasmic PAR-2, which increases the on rate in the inhibited zone. The attaching PAR-2 then diffuses, out-competing the PAR-3 and driving it to a lower steady state. This shifts the boundary, as previously observed in [4].
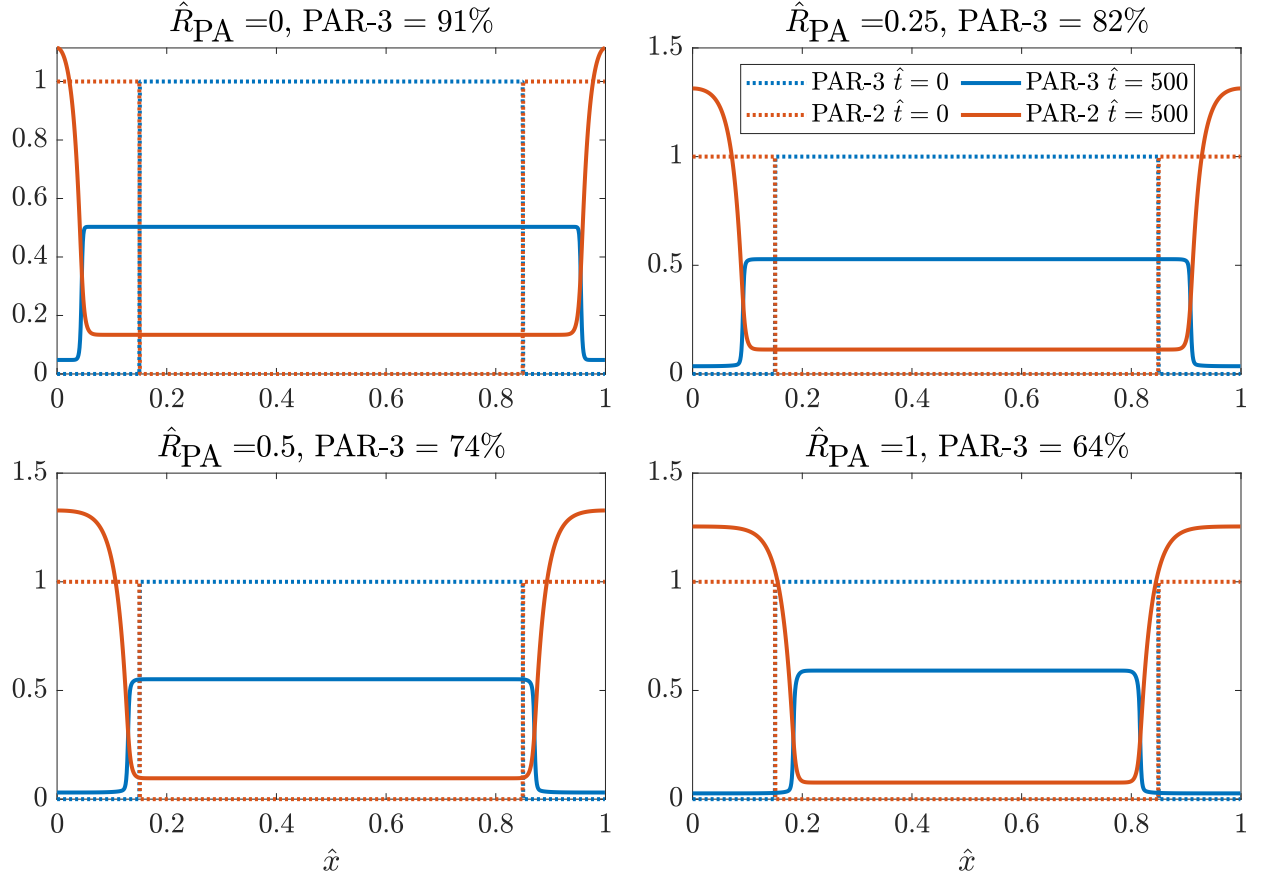
20

Figure 9: Steady states ($\hat{t} = 500$) of the PAR-2/PAR-3 model (23) with various values of $\hat{R}_{\text{PA}}$ (P inhibits A). The dotted blue and red lines shows the initial distribution of PAR-3 and PAR-2 (respectively) in each case, and the solid lines show the steady state at $\hat{t} = 500$. The title indicates the strength that P inhibits A, which is $\hat{R}_{\text{PA}}$, and also the resulting size of the PAR-3 domain.
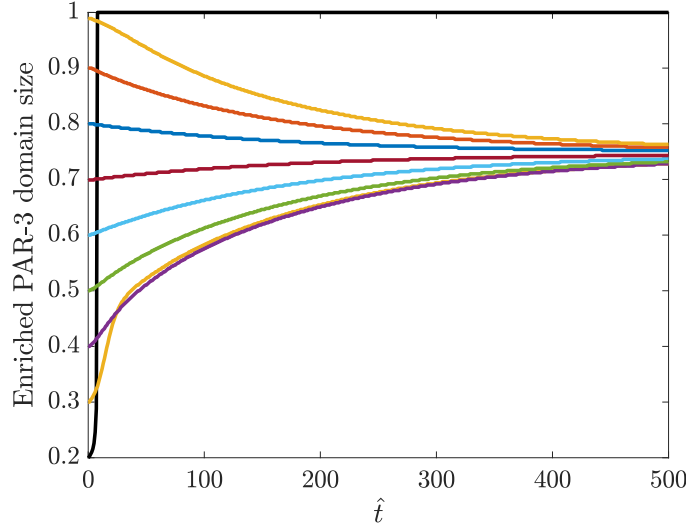
Figure 10: Size of the PAR-3 enrichment zone over time. Simulations use parameters in Table 2 and 3 and start with $\hat{A} = 1$ and $\hat{P} = 0$ in an enrichment zone (as in the bottom row of Fig. 9). We then watch the size of the domain evolve over time. If there is sufficient cytoplasmic depletion of PAR-3, then mutual inhibition by PAR-2 shifts the intrinsic boundary.

2.5.2 Steady state

Because of the experimental observation that embryos depleted of myosin have about 75% PAR-3 enrichment at the end of maintenance [17, Fig. 5B], we set $\hat{R}_{\mathrm{PA}} = 0.5$, which is the bottom left plot in Fig. 9. In this steady state, we have about 5% (0.03/0.54) PAR-3 on the posterior relative to the anterior, and 7% (0.1/1.4) PAR-2 on the anterior relative to the posterior. These roughly correspond to experimental observations, although the changes in the PAR-3 concentration (from 10% to 5%) are not as drastic as those observed experimentally [14, Fig. 4C].

2.5.3 Approach to steady state

We now demonstrate that the steady state boundary position is set uniquely by the parameters. When $\hat{R}_{\mathrm{AP}} = 100$ and $\hat{R}_{\mathrm{PA}} = 0.5$, Fig. 9 shows that the domain of PAR-3 enrichment at steady state is roughly 75%. We confirm that this is a unique steady state in Fig. 10 by changing length of the region initially enriched in PAR-3. We find that, as long as the domain size is larger than 0.2, we see a unique steady state where PAR-3 and PAR-2 mutually exclude each other. By contrast, when the initial domain of enrichment is too small, there is sufficient cytoplasmic PAR-3 for the uniform steady state to be the only stable one. These dynamics are similar to the case of PAR-3
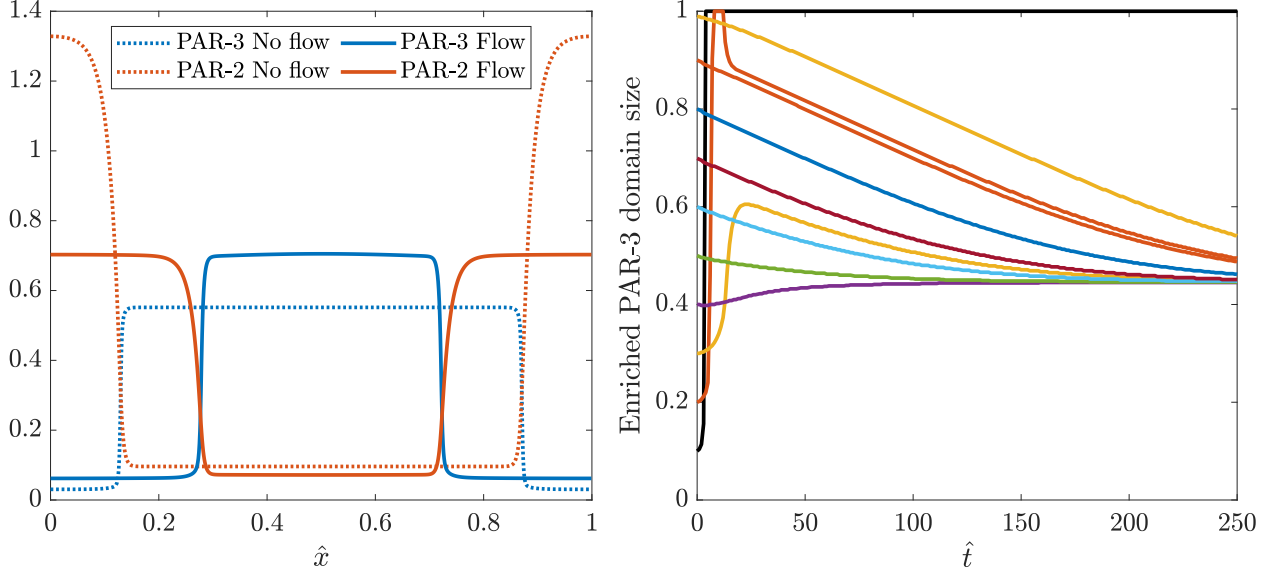
Figure 11: Augmenting the biochemistry model with the steady state maintenance phase flow in *arx-2* (RNAi) embryos (see Fig. 2). The left panel compares the steady states with PAR competition vs. the steady states with the experimental flow field. There is an enrichment of aPARs and depletion of pPARs as the boundary contracts inward. The speed of contraction for different initial conditions is shown at right.

alone (Fig. 7), except that inhibition by PAR-2 increases the range of cytoplasmic concentrations for which bistability exists.

We note also that, as in the intrinsic PAR-3 dynamics, the approach to steady state is quite slow, as it is contolled by the diffusion of PAR-3 monomers and PAR-2. Indeed, Fig. 10 shows that, in 10 minutes of real time ($\hat{t} = 48$), the enriched PAR-3 domain changes by at most 5–10%.

2.5.4 With the experimental myosin profile

To illustrate what happens when we add flow, we now add to the simulation the experimental flow profile in embryos depleted of branched actin, depicted in Fig. 2. The model equations are identical to (24), except that the flow profile $\hat{v}$ is imposed from the experimental measurement in Fig. 2 and not computed internally. Figure 11 shows the resulting steady state and the approach to it from different initial zones of PAR-2/3 enrichment. We see two major results: first, the boundary has shifted from 75% PAR-3 enrichment to roughly 45%, as is typical in the *arx*-2 embryos. Second, the approach to the steady state is faster. Even though the boundary has to shift farther, the steady state is reached in almost all cases by $\hat{t} = 250$, as now flow *and* diffusion control how long it takes to get there. Indeed, for the boundary to move 30% of the domain length on each side, it needs to
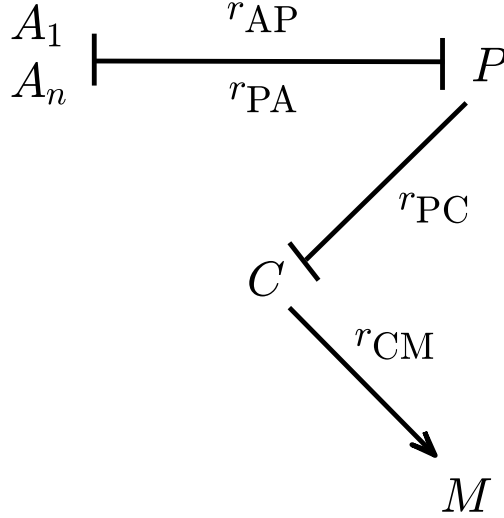
Figure 12: Model schematic for this section. A_1 and A_n represent PAR-3 monomers and oligomers, as well as PAR-6 and PKC-3. P represents pPARs, C represents CDC-42, and M represents myosin.

move 40 μm. Since the maximum flow speed is 1 μm/min, we expect 40 minutes, or 2400 seconds, or $\hat{t} \approx 200$ to be the time it takes to shift the boundary to steady state. This is indeed what we see in the right panel of Fig. 11. This indicates that flow dominates the approach to steady state.

3   Coupling contractility to biochemistry

We now present the full model with contractility and all of the biochemistry, as shown in Fig. 12. We will again have two protein species A (representing PAR-3) and P (representing PAR-2), which mutually inhibit each other. The actual inhibition of PAR-2 comes from PAR-6 and PKC-3, which colocalize with PAR-3 and are therefore not represented here. Likewise, the posterior protein which inhibits PAR-3 is actually PAR-1, which colocalizes with PAR-2 and is also therefore not represented. The mutual inhibition strengths for A and P were determined in Section 2.5.1, so we don't need to fit any parameters associated with these proteins.

The goal of this section is to couple the dynamics of proteins to myosin. We do this through the GTPase CDC-42, which activates myosin and branched actin. CDC-42 is typically enriched in the anterior (it is an aPAR), because it is inhibited in the posterior by its GAP, CHIN-1 [14]. As shown in Fig. 12, we model this by introducing the species C, which represents CDC-42 and is inhibited by P, and reintroducing myosin M from Section 1.

Parameter	Description	Value	Units	Ref	Notes
D_C	C diffusivity	0.1	$\mu\text{m}^2/\text{s}$	[12]	Known (PAR-6)
k_C^{off}	C detachment rate	0.01	$1/\text{s}$	[12]	Known (PAR-6)
k_C^{on}	C attachment rate	0.1	$\mu\text{m}/\text{s}$		50% bound C no inhibition
k_M^{on}	M attachment rate	0.3	$\mu\text{m}/\text{s}$		20% bound M no CDC
$\hat{R}_{\text{PC}}$	P inhibiting C	27.3		[14]	CDC/CHIN-1 relationship (Fig. A5)
$\hat{R}_{\text{CM}}$	C promoting M	0.75			Correct M profile

Table 4: Additional parameters and fitting parameters for coupled model shown in Fig. 12.

3.1 Dimensionless equations

The dimensionless equations that govern the schematic shown in Fig. 12 are

$$\partial_{\hat{t}}\hat{A}_1 + \hat{\sigma}_0\partial_{\hat{x}}\left(\hat{v}\hat{A}_1\right) = \hat{D}_A\partial_{\hat{x}}^2 A_1 + \hat{K}_A^{\text{on}}\left(1 + \hat{K}_A^+ F_A^+\left(\hat{A}_1, \hat{A}_n\right)\right)\left(1 - \int_0^1 \hat{A}(x)\,d\hat{x}\right)$$
$$+ 2\hat{K}_A^{\text{dp}}\hat{A}_n - 2\hat{K}_A^{\text{p}}\hat{A}_1^{\;2} - \hat{K}_A^{\text{off}}\hat{A}_1 \tag{24a}$$

$$\partial_{\hat{t}}\hat{A}_n + \hat{\sigma}_0\partial_{\hat{x}}\left(\hat{v}\hat{A}_n\right) = \hat{K}_A^{\text{p}}\hat{A}_1^{\;2} - \hat{K}_A^{\text{dp}}\left(1 + \hat{R}_{\text{PA}}\hat{P}\right)\hat{A}_n \tag{24b}$$

$$\partial_{\hat{t}}\hat{P} + \hat{\sigma}_0\partial_{\hat{x}}\left(\hat{v}\hat{P}\right) = \hat{D}_P\partial_{\hat{x}}^2\hat{P} + \hat{K}_P^{\text{on}}\left(1 - \int_0^1 \hat{P}(\hat{x})\,d\hat{x}\right) - \hat{K}_P^{\text{off}}\left(1 + \hat{R}_{\text{AP}}\hat{A}\right)\hat{P} \tag{24c}$$

$$\partial_{\hat{t}}\hat{C} + \hat{\sigma}_0\partial_{\hat{x}}\left(\hat{v}\hat{C}\right) = \hat{D}_C\partial_{\hat{x}}^2\hat{C} + \hat{K}_C^{\text{on}}\left(1 - \int_0^1 \hat{C}(\hat{x})\,d\hat{x}\right) - \hat{K}_C^{\text{off}}\left(1 + \hat{R}_{\text{PC}}\hat{P}\right)\hat{C} \tag{24d}$$

$$\partial_{\hat{t}}\hat{M} + \hat{\sigma}_0\partial_{\hat{x}}\left(\hat{v}\hat{M}\right) = \hat{D}_M\partial_{\hat{x}}^2\hat{M} + \hat{K}_M^{\text{on}}\left(1 + \hat{R}_{\text{CM}}\hat{C}\right)\left(1 - \int_0^1 \hat{M}(x)\,dx\right) - \hat{K}_M^{\text{off}}\hat{M} \tag{24e}$$

$$\hat{v} = \hat{\ell}^2\partial_{\hat{x}}^2 v + \hat{\ell}\partial_{\hat{x}}\hat{\sigma}_a(\hat{M}) \tag{24f}$$

$$R_{\text{CM}} = \frac{r_{\text{CM}}C^{(\text{Tot})}}{k_M^{\text{on}}}, \quad \hat{R}_{\text{PC}} = \frac{r_{\text{PC}}P^{(\text{Tot})}}{k_C^{\text{off}}}, \quad \hat{D}_C = \frac{D_C}{L^2 k_A^{\text{dp}}}, \quad \hat{K}_C^{\text{on}} = \frac{k_C^{\text{on}}}{k_A^{\text{dp}}h}, \quad \hat{K}_C^{\text{off}} = \frac{k_C^{\text{off}}}{k_A^{\text{dp}}} \tag{24g}$$

These equations combine the equations (9a) for myosin with the A/P cross-inhibitory circuit (23), adding CDC-42 as the species C. In doing this, we introduce five new dimensionless parameters in (24g).

3.2 Parameter estimation

The diffusivity and unbinding rate of PAR-6 have been measured in [12]. If we assume that CDC-42 and PAR-6 have similar properties, this sets D_C and k_C^{off} as given in Table 4. There are then four unknown parameters: the on rates for CDC-42 k_C^{on} and myosin k_M^{on}, the rate at which P inhibits C, and the rate at which C promotes M. We set these parameters based on the following observations.

1. In [5, Fig. S3i], it is reported that roughly 25% of PAR-6 is bound in wild-type embryos. Assuming that CDC-42 has a similar set of properties, we can assume 25% of the protein is bound. Since the posterior half will be inhibited by CHIN-1, we look for about 50% of the protein bound without inhibition. This sets k_C^{on} via $k_C^{\text{on}}/(k_C^{\text{on}} + k_C^{\text{off}}h) = 0.5$, giving $k_C^{\text{on}} = 0.1$ μm/s.

2. The parameter $\hat{R}_{\text{PC}}$ is available from the data in [14]. To obtain it, we solve (24d) at steady state in the absence of A to obtain

$$\hat{C} = \frac{1}{1 + \frac{hk_c^{\text{off}}}{k_C^{\text{on}}} + \frac{\hat{R}_{\text{PC}}k_C^{\text{off}}h}{k_C^{\text{on}}}\hat{P}}. \tag{25}$$

Now according to [14], in a system of units where $\hat{C} = 1$ when $\hat{P} = 0$,

$$\tilde{C} = \frac{1 + \frac{hk_c^{\text{off}}}{k_C^{\text{on}}}}{1 + \frac{hk_c^{\text{off}}}{k_C^{\text{on}}} + \frac{\hat{R}_{\text{PC}}k_C^{\text{off}}h}{k_C^{\text{on}}}\hat{P}}$$

we have $\hat{C} \approx 1/(1 + 13.3\hat{P})$, which implies that

$$13.3 = \frac{\hat{R}_{\text{PC}}k_C^{\text{off}}h}{k_C^{\text{on}}\left(1 + \frac{hk_c^{\text{off}}}{k_C^{\text{on}}}\right)} = \frac{\hat{R}_{\text{PC}}k_C^{\text{off}}h}{k_C^{\text{on}} + hk_c^{\text{off}}} \rightarrow \hat{R}_{\text{PC}} = 27.3$$

3. In wild-type and *arx-2* (RNAi) embryos, the minimum amount of bound myosin is 0.2. This sets k_M^{on} via $k_M^{\text{on}}/(k_M^{\text{on}} + k_M^{\text{off}}h) = 0.2$, giving $k_M^{\text{on}} = 0.3$ μm/s.

4. We then fit the parameter $\hat{R}_{\text{CM}} = 0.75$ to match the boundary position in *arx-2* (RNAi) embryos, as shown in Fig. 2.

3.3 The steady state compared to experiments

We now look at the performance of this model compared to the experimental data. We simulate the model (24) (with parameters in Table 4) to steady state, and plot the results in Fig. 13. The left panel shows the steady state, where roughly 40% of the domain is taken up by PAR-3. The next two panels show how the myosin intensity and flow profiles compare with the experimental data. At the correct boundary position, the flow profile that we obtain (right panel) matches with the experimental data for *arx-2* (RNAi), but not wild-type embryos. Wild-type embryos tend to have a higher absolute flow speed at steady state, and the peak flow actually occurs in the *posterior* domain, with the flow speed in most of the anterior domain ($\hat{x} = 0.25$ to $\hat{x} = 0.45$) being zero.
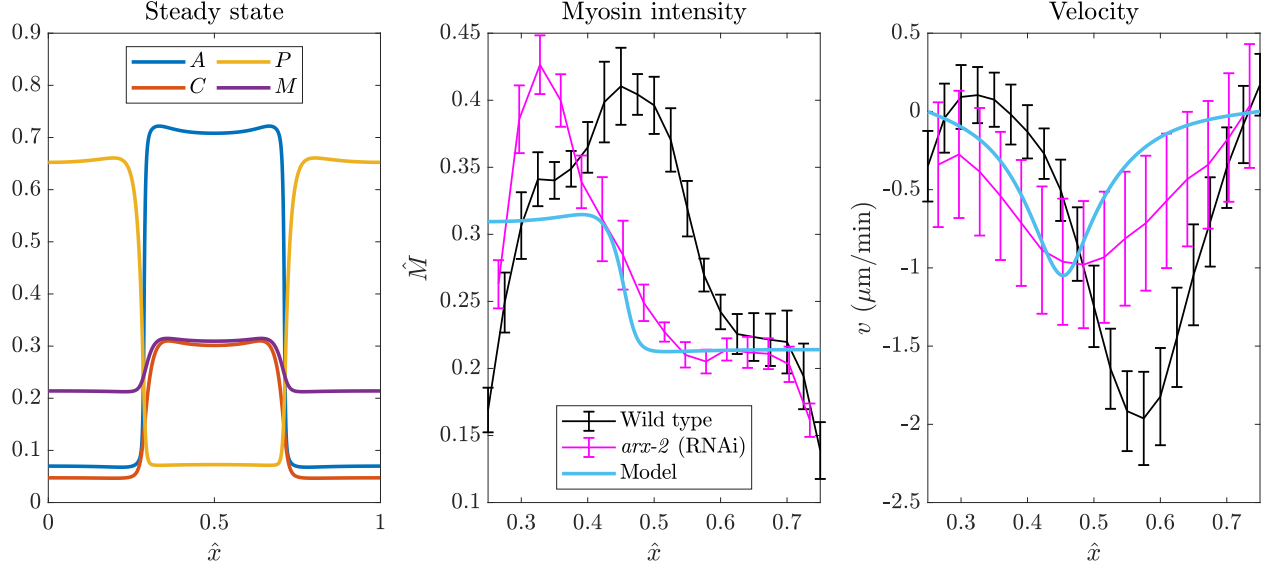
Figure 13: Steady state of the model (24), compared to experimental results. The left panel shows the steady state aPAR, pPAR, CDC-42, and myosin levels along the embryo length, with the anterior pole at $\hat{x}$0.5. The middle and rightmost plots show the comparison with experimental data. We show wild-type embryos in black, and *arx-2* (RNAi) embryos in pink. Results of the model (shifting the anterior pole to $\hat{x} = 0.25$) are ovelaid with the experimental data.

The stalling of the flow in the anterior domain of wild-type embryos corresponds to a peak in the myosin intensity curve around $\hat{x} = 0.5$, after which we see a decrease that is not due to imaging artifacts (black curve in the middle plot).

Our conclusion from this section is that our model can successfully reproduce the dynamics in *arx-2* (RNAi) embryos, but not in wild type ones. This tells us that we need to incorporate branched actin into the model to see how it might be responsible for the flow and myosin intensity curves. Of course, even for *arx-2* (RNAi) embryos the model is not perfect. It gives a sharper slope in the myosin intensity curve than the experimental data, which means a smaller increase in intensity is needed to reproduce the same velocity. Nevertheless, we declare the results "good enough" to move on to branched actin.

3.4 Incorporating branched actin

Let's suppose

$$\partial_{\hat{t}}\hat{M} + \hat{\sigma}_0\partial_{\hat{x}}\left(\hat{v}\hat{M}\right) = \hat{D}_M\partial_{\hat{x}}^2\hat{M} + \hat{K}_M^{\mathrm{on}}\left(1 + \hat{R}_{\mathrm{CM}}\hat{C}\right)\left(1 - \int_0^1 \hat{M}(x)\,dx\right) - \hat{K}_M^{\mathrm{off}}\hat{M} \qquad (24\mathrm{e})$$

27

References

[1] Tom Bland, Nisha Hirani, David Briggs, Riccardo Rossetto, KangBo Ng, Neil Q McDonald, David Zwicker, and Nathan W Goehring. Optimized dimerization of the par-2 ring domain drives cooperative and selective membrane recruitment for robust feedback-driven cell polarization. *bioRxiv*, pages 2023–08, 2023.

[2] Justin S Bois, Frank Jülicher, and Stephan W Grill. Pattern formation in active fluids. *Biophysical Journal*, 100(3):445a, 2011.

[3] Adriana T Dawes and Edwin M Munro. Par-3 oligomerization may provide an actin-independent mechanism to maintain distinct par protein domains in the early caenorhabditis elegans embryo. *Biophysical journal*, 101(6):1412–1422, 2011.

[4] Nathan W Goehring, Philipp Khuc Trong, Justin S Bois, Debanjan Chowdhury, Ernesto M Nicola, Anthony A Hyman, and Stephan W Grill. Polarization of par proteins by advective triggering of a pattern-forming system. *Science*, 334(6059):1137–1141, 2011.

[5] Peter Gross, K Vijay Kumar, Nathan W Goehring, Justin S Bois, Carsten Hoege, Frank Jülicher, and Stephan W Grill. Guiding self-organized pattern formation in cell polarity establishment. *Nature physics*, 15(3):293–300, 2019.

[6] Jacob Halatek, Fridtjof Brauns, and Erwin Frey. Self-organization principles of intracellular pattern formation. *Philosophical Transactions of the Royal Society B: Biological Sciences*, 373(1747):20170107, 2018.

[7] Rukshala Illukkumbura, Nisha Hirani, Joana Borrego-Pinto, Tom Bland, KangBo Ng, Lars Hubatsch, Jessica McQuade, Robert G Endres, and Nathan W Goehring. Design principles for selective polarization of par proteins by cortical flows. *Journal of Cell Biology*, 222(8), 2023.

[8] Charles F Lang, Alexander Anneken, and Edwin Munro. Oligomerization and feedback on membrane recruitment stabilize par-3 asymmetries in c. elegans zygotes. *bioRxiv*, pages 2023–08, 2023.

[9] Charles F Lang and Edwin Munro. The par proteins: from molecular circuits to dynamic self-stabilizing cell polarity. *Development*, 144(19):3405–3416, 2017.

[10] Charles F Lang and Edwin M Munro. Oligomerization of peripheral membrane proteins provides tunable control of cell surface polarity. *Biophysical Journal*, 121(23):4543–4559, 2022.

[11] Alex Mogilner, Jun Allard, and Roy Wollman. Cell polarity: quantitative modeling as a tool in cell biology. *Science*, 336(6078):175–179, 2012.

[12] François B Robin, William M McFadden, Baixue Yao, and Edwin M Munro. Single-molecule analysis of cell surface dynamics in caenorhabditis elegans embryos. *Nature methods*, 11(6):677–682, 2014.

[13] Arnab Saha, Masatoshi Nishikawa, Martin Behrndt, Carl-Philipp Heisenberg, Frank Jülicher, and Stephan W Grill. Determining physical properties of the cell cortex. *Biophysical journal*, 110(6):1421–1429, 2016.

[14] Anne Sailer, Alexander Anneken, Younan Li, Sam Lee, and Edwin Munro. Dynamic opposition of clustered proteins stabilizes cortical polarity in the c. elegans zygote. *Developmental cell*, 35(1):131–142, 2015.

[15] Filipe Tostevin and Martin Howard. Modeling the establishment of par protein polarity in the one-cell c. elegans embryo. *Biophysical journal*, 95(10):4512–4522, 2008.

[16] Philipp Khuc Trong, Ernesto M Nicola, Nathan W Goehring, K Vijay Kumar, and Stephan W Grill. Parameter-space topology of models for cell polarity. *New Journal of Physics*, 16(6):065009, 2014.

[17] Seth Zonies, Fumio Motegi, Yingsong Hao, and Geraldine Seydoux. Symmetry breaking and polarization of the c. elegans zygote by the polarity protein par-2. *Development*, 137(10):1669–1677, 2010.